Posture-Dependent Collapse of the Optic Nerve Subarachnoid Space: A Combined MRI and Modeling Study

Petter Holmlund,[1] Karen-Helene Støverud,[1] Anders Wåhlin,[1,2] Urban Wiklund,[1] Jan Malm,[3] Gauti Jóhannesson,[4,5] and Anders Eklund[1,2]

[1]Department of Radiation Sciences, Umeå University, Umeå, Sweden
[2]Umeå Center for Functional Brain Imaging, Umeå University, Umeå, Sweden
[3]Department of Clinical Science, Neurosciences, Umeå University, Umeå, Sweden
[4]Department of Clinical Sciences, Ophthalmology, Umeå University, Umeå, Sweden
[5]Wallenberg Centre for Molecular Medicine, Umeå University, Umeå, Sweden

Correspondence: Petter Holmlund, Department of Radiation Sciences, Umeå University, 901 87 Umeå, Sweden; petter.holmlund@umu.se.

PH and KHS contributed equally.

Received: November 28, 2020
Accepted: March 20, 2021
Published: April 20, 2021

Citation: Holmlund P, Støverud K-H, Wåhlin A, et al. Posture-dependent collapse of the optic nerve subarachnoid space: A combined MRI and modeling study. *Invest Ophthalmol Vis Sci.* 2021;62(4):26. https://doi.org/10.1167/iovs.62.4.26

Purpose. We hypothesize that a collapse of the optic nerve subarachnoid space (ONSAS) in the upright posture may protect the eyes from large translamina cribrosa pressure differences (TLCPD) believed to play a role in various optic nerve diseases (e.g., glaucoma). In this study, we combined magnetic resonance imaging (MRI) and mathematical modeling to investigate this potential ONSAS collapse and its effects on the TLCPD.

Methods. First, we performed MRI on six healthy volunteers in 6° head-down tilt (HDT) and 13° head-up tilt (HUT) to assess changes in ONSAS volume (measured from the eye to the optic canal) with changes in posture. The volume change reflects optic nerve sheath (ONS) distensibility. Second, we used the MRI data and mathematical modeling to simulate ONSAS pressure and the potential ONSAS collapse in a 90° upright posture.

Results. The MRI showed a 33% decrease in ONSAS volume from the HDT to HUT ($P < 0.001$). In the upright posture, the simulations predicted an ONSAS collapse 25 mm behind lamina cribrosa, disrupting the pressure communication between the ONSAS and the intracranial subarachnoid space. The collapse reduced the simulated postural increase in TLCPD by roughly 1 mm Hg, although this reduction was highly sensitive to ONS distensibility, varying between 0 and 4.8 mm Hg when varying the distensibility by ± 1 SD.

Conclusions. The ONSAS volume along the optic nerve is posture dependent. The simulations supported the hypothesized ONSAS collapse in the upright posture and showed that even small changes in ONS stiffness/distensibility may affect the TLCPD.

Keywords: glymphatics, optic nerve subarachnoid space, translaminar pressure, glaucoma, posture

Abnormal pressure differences between the intraocular and intracranial space, that is, the translamina cribrosa pressure difference (TLCPD), and its posture dependency, have been hypothesized to play an important role in optic nerve diseases, including normal tension glaucoma[1–4] and idiopathic intracranial hypertension.[5–7] In addition, deviations in the TLCPD may also be related to visual disturbances found among astronauts exposed to microgravity and development of the spaceflight-associated neuro-ocular syndrome.[7–10]

In the supine position, the intracranial subarachnoid space (SAS) is expected to be in direct fluid contact with the optic nerve SAS (ONSAS), implying that the TLCPD can be assessed from intraocular pressure (IOP) and intracranial pressure (ICP). When moving to upright postures, the ICP decreases much more than the IOP, inferring a much larger TLCPD when sitting/standing.[7] Increased TLCPD generates an elevated mechanical bending force on the lamina cribrosa (LC). However, experimental animal studies[11,12] have indicated that the ICP and ONSAS pressures are directly correlated only as long as the ICP is above a certain threshold, roughly larger than 0 mm Hg. These results suggest that below this limit, the ONSAS collapses because of low ICP, effectively disrupting the communication between the ONSAS and the cranial SAS. In humans, an ONSAS collapse may thus protect the eye from large TLCPDs when standing/sitting up,[5] as ICP likely drops below the orbital tissue pressure surrounding the ONSAS in more upright body postures.[12,13] So far, no study has investigated posture-related effects on the relationship between ICP and the pressure in the ONSAS, nor the effects of a posture-related ONSAS collapse on the TLCPD.

Simultaneous assessment of ICP and ONSAS pressure in vivo in humans is highly challenging because pressure measurements in the ONSAS are extremely risky. Therefore in the current study, we used a combination of magnetic

resonance imaging (MRI) and mathematical modeling to calculate these pressures and to investigate the potential posture-driven collapse of the ONSAS. The study consisted of two parts. First, we utilized MRI of healthy volunteers in a 6° head-down tilt (HDT) and a 13° head-up tilt (HUT) body position to directly assess changes in ONSAS volume with changes in posture, reflecting optic nerve sheath (ONS) distensibility. Then we used the data from the MRI as input to a mathematical model of the cerebrospinal fluid (CSF) circulation, including the craniospinal SAS and the ONSAS, for determination of the ONSAS pressure and to simulate the potential collapse in a full 90° upright body posture.

Methods

MRI of the ONSAS

Subjects. Six healthy volunteers were included for MRI investigations (2 women, 4 men, age mean ± SD: 49 ± 9 years). The subjects had no neurologic or ophthalmologic diseases and were not taking any medications affecting the central nervous system. Their IOP was normal (14 ± 2 mm Hg in the supine posture, 10 ± 1 mm Hg in a sitting position). The study was performed in accordance with the Declaration of Helsinki. All participants signed an informed consent form, and the study was approved by the regional ethical review board in Umeå (approval no. 2014/223-31).

MRI Sequence and Protocol. The subjects were scanned using a 3T scanner (GE Discovery MR750; General Electric Healthcare, Waukesha, WI, USA) using a 32-channel head coil. The ONSAS was imaged using a T2-weighted fast recovery fast spin echo sequence with fat suppression,[14,15] and the MRI sequence was optimized to detect the ONSAS. The volume of interest was positioned so that the slices were perpendicular to the optic nerve in the orbital section of the nerve (resulting in oblique coronal images). The settings were repetition time/echo time 6000/196 ms; number of excitations 3; flip angle 111°; echo-train length 24; pixel bandwidth 195.312 Hz/pixel; field of view 160 x 160 mm; matrix 512 × 512; slice thickness 2 mm; slice gap 0; number of slices 25; scanning time 2:30 min:sec. This resulted in a volume of 160 × 160 × 50 mm^3 with a resolution of 0.31 x 0.31 x 2 mm. The scans covered a distance from the eye all the way to the intracranial part of the optic nerve. The MRIs were performed in two different body positions: a HDT position of tilt-angle –5.8°, and a HUT position of tilt-angle +13.3° (maximum achievable in the scanner). The HUT position was achieved by using a wedge to lift the upper body of the research subjects and by tilting the head coil toward the roof of the camera. The subjects were positioned 5 to 10 minutes before the scans started. Each eye was scanned twice, with the scan with the highest signal to noise ratio being used for the analyses. The scans started with the right eye and continued with the left eye. The order of the HDT and HUT scans was randomized (three subjects started in HDT and three in HUT). The difference in ONSAS pressure between the HDT and HUT positions was estimated by measuring the change in height of the ONSAS (at the level of the LC) between the two body positions, with reference to the heart.

Segmentation of the ONSAS. The ONSAS volume all the way from the LC to the optic canal was directly acquired from the MRIs. The ONSAS was manually segmented using ScanIP from Synopsys' Simpleware software (Version M-2017.06; Synopsys Inc., Mountain View, CA, USA). One investigator segmented the ONSAS for all subjects, whereas a second investigator repeated half of the measurements (randomized and blinded to body posture status) to assess the inter-rater agreement (intraclass correlation coefficient [ICC] = 0.92, indicating excellent agreement).

From the segmentations, the cross-sectional area of the ONSAS was acquired for each slice (A_i^{HDT} and A_i^{HUT}), see Figure 1A, with i indicating the slice/segment number, reflecting the distance from the LC. Multiplying the areas by slice thickness yielded the corresponding volumes (V_i^{HDT} and V_i^{HUT}). Furthermore, the radius of the ONSAS in HDT ($r_{ONS_i}^{HDT}$) was also assessed from the MRIs for each slice (Fig. 1B). Assuming the ONSAS is shaped like an annulus, the radius of the optic nerve (r_{ONi}) followed directly from A_i^{HDT} and $r_{ONS_i}^{HDT}$. The ONSAS radius in HUT ($r_{ONS_i}^{HUT}$) was then directly acquired from A_i^{HUT} and r_{ONi}. The ONS distensibility was given by the local change in radius per unit pressure:

$$D_i = \frac{\Delta r_i}{\Delta P} = \frac{r_{ONS_i}^{HDT} - r_{ONS_i}^{HUT}}{P_{ONSAS_{HDT}} - P_{ONSAS_{HUT}}}, \quad (1)$$

where D_i is the distensibility of the ONS and $P_{ONSAS_{HDT}} - P_{ONSAS_{HUT}}$ is the change in ONSAS pressure between HDT

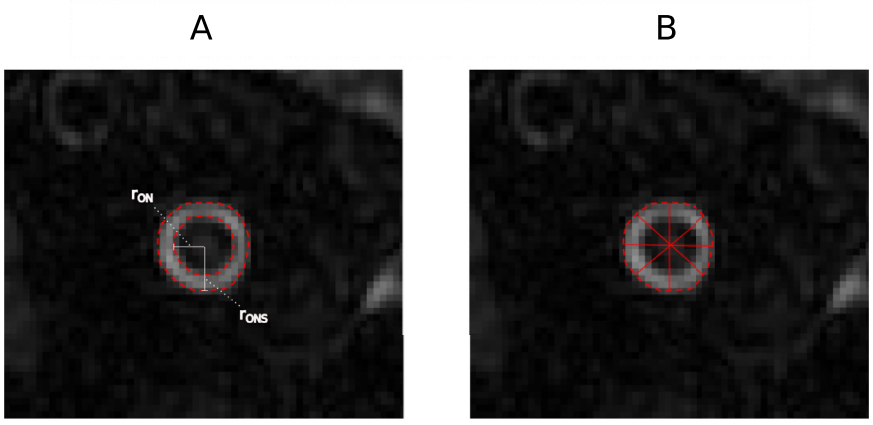

Figure 1. MRI image of the ONSAS segmentation. (**A**) Volume. (**B**) Diameter (average of four directions). The ONSAS radius r_{ONS} and optic nerve radius r_{ON} are also highlighted.

Investigative Ophthalmology & Visual Science

Table 1. Distensibility, ONSAS Radii, and Optic Nerve Radii Along the Extension of the Optic Nerve (Means of All 12 Nerves)

Region	MRI Slice	$r_{ONS_i}^{HDT}$	r_{ON_i}	$r_{ONS_i}^{HUT}$	L_i	D_i
Units	**[ ]**	mm	mm	mm	mm	mm/mm Hg
Bulbar	1	2.67	1.76	2.46	2	0.02
	2	2.86	1.77	2.60	2	0.027
	3	2.61	1.79	2.37	2	0.024
	4	2.34	1.67	2.10	2	0.024
Midorbital	5	2.11	1.56	1.96	2	0.015
	6	1.98	1.48	1.83	2	0.015
	7	1.92	1.41	1.74	2	0.017
	8	1.90	1.39	1.72	2	0.017
	9	1.91	1.43	1.77	2	0.014
	10	1.88	1.48	1.73	2	0.015
	11	1.80	1.49	1.69	2	0.011
	12	1.79	1.54	1.67	2	0.013
	13	1.78	1.53	1.63	2	0.016

and HUT. The radii and the distensibility for each slice are presented in Table 1.

Mathematical Modeling of the CSF Circulation

Compartment Model. The compartment model suggested in this study is based on the work previously presented by Gehlen et al.[16] who modeled the CSF circulation with changes in posture. Their model included two compartments for the cranio-spinal CSF space, one for the cranial part and one for the spinal part, successfully describing ICP and CSF volume redistribution during the transition from supine to upright postures. The model included a constant production of CSF in the choroid plexus and a pressure driven absorption to venous blood through arachnoid granulations (AGs),[17] and incorporated the effects of the collapsible jugular veins on the CSF dynamics in the upright posture.[16,18,19] In the current study, we further developed the model by Gehlen et al.[16] into a three-compartment model by adding the ONSAS as a separate compartment together with an additional CSF absorption route through the ONS.[20–22] This allowed for CSF volume and pressure to be transferred between the intracranial SAS and the ONSAS, thus connecting the ICP to the ONSAS pressure (P_{ONSAS}). Importantly, the flow resistance between the cranial SAS and ONSAS compartments (R_{ONSAS}) was based on our collected MRI data (described in the previous section), opening for a potentially collapsible ONSAS. For an overview of the compartment model, see Figure 2. The new additions to the model are summarized in Table 2. Details for the craniospinal part of the model can be found in the article by Gehlen et al.,[16] whereas our input parameters to the model are presented under Supplementary materials (Supplementary Table S1).

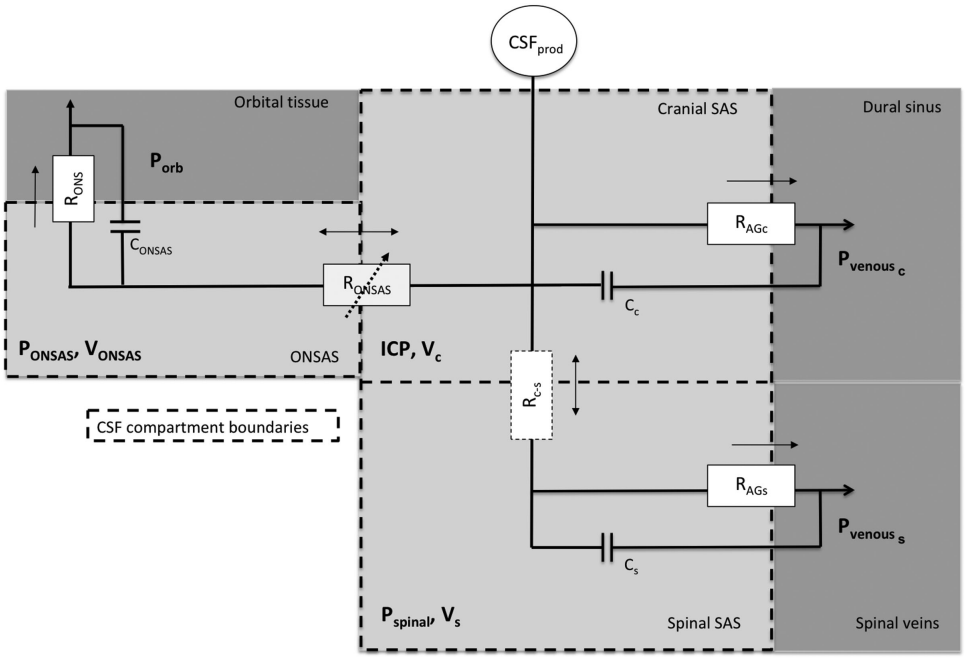

Figure 2. The compartment model. The three compartments consist of the cranial SAS (c), spinal SAS (s), and ONSAS, each with a pressure, volume, and compliance. Changes in volume from supine equilibrium in each compartment serve as the dependent variables of the underlying ordinary differential equations (ODEs) of the model. The model includes cranial CSF production and CSF absorption to the venous system through arachnoid granulations (AG) and absorption across the ONS. Flow rates (*indicated by arrows*) are determined by the pressure difference and resistances between compartments. For all absorption sites, only outflow from the CSF compartments was allowed. The compliances depend on both internal CSF pressures and surrounding venous (and intraorbital) pressures, meaning that venous pressure plays a major role both in absorption and compliance. The ONSAS resistance (R_{ONSAS}) is based on the acquired MRI measurements of the ONSAS/ONS radius (r_{ONS}) and is allowed to vary. Postural changes are implemented through hydrostatic effects in the CSF and venous systems, including the collapse of the internal jugular veins and the potential collapse of the ONSAS. The reference level for compartment *c* is the auditory meatus,[7] the venous hydrostatic indifference point[18] is used for compartment *s*, and the level of the LC for the ONSAS compartment. The pressures were hydrostatically adjusted to the same level when calculating the flow rates to account for the height differences between the reference points. The main model outputs include ICP at the level of the LC (ICP_{LC}), the ONSAS pressure (P_{ONSAS}) and r_{ONS} when going from supine to upright.

Investigative Ophthalmology & Visual Science

Table 2. Summary of the New Additions Introduced in the Current Model

1) A separate compartment for the ONSAS
2) A variable ONSAS resistance based on ONS distensibility
3) An additional outflow of CSF across the ONS
4) Changes in body posture can be performed in a continuous fashion
5) Includes effects of viscous resistances along the venous system (even in supine)

Modeling the ONSAS Radius Using the MRI Data. We separated the ONSAS into three main regions: bulbar, orbital, and canicular. For the canicular part of the ONSAS, the ONS radius was kept *constant*, that is, $r_{ONS_C} = r_{ONS_C}^{HDT} = 1.78\ mm$, whereas for the bulbar and orbital parts, r_{ONS} is pressure dependent and thus the resistance to CSF flow from the intracranial to the ONSAS compartment will increase with decreasing radius. As our achieved HUT in the MRI did not extend to 90°, we assumed D_i to be constant within the pressure range of the full posture change from supine to upright. From Equation (1), we then calculated the radii as a function of pressure

$$r_{ONS_i} = r_{ONS_i}^{HDT} + D_i \cdot \left(P_{ONSAS} - P_{ONSAS_{HDT}}\right). \quad (2)$$

This is an important feature of the model because it allows us to study the potential collapse of the ONSAS. When sitting up, $P_{ONSAS} - P_{ONSAS_{HDT}}$ becomes negative, and at some point, if it becomes negative enough, r_{ONS} reaches r_{ON}, which indicates collapse.

In the current study, we neglected the trabeculae, pillars, and septae in the ONSAS and calculated the axial flow resistance in the ONSAS based on Poiseuille flow in an annulus:

$$R_{ONSAS_i} = \frac{8\mu}{\pi r_{ON_i}^4} \cdot \left(\frac{L_i}{k_i^4 - 1 - \frac{(k_i^2-1)^2}{ln(k_i)}}\right), \quad (3)$$

where $k_i = \frac{r_{ONS_i}}{r_{ON_i}}$, μ is the CSF viscosity, L_i is the length of each segment in ONSAS. We divided the bulbar and orbital ONSAS into 13 segments with a thickness of 2 mm, that is, the same resolution as the MRI data. The resulting ONSAS length (L_{ONSAS}) was 26 mm, extending from the LC to the optic canal.

The total compliance for the ONSAS was calculated as:

$$C_{ONSAS} = \frac{\Delta V_{ONSAS}}{\Delta P_{ONSAS}} = 2\pi L_{ONSAS} \bar{r}_{ONS} \bar{D}, \quad (4)$$

where $\bar{r}_{ONS}$ is the (average) radius along the ONSAS, and $\bar{D}$ is the average distensibility as given by the mean of all segments in Equation (1). Equation (4) followed from the assumption of an annular ONSAS.

ONS Outflow Resistance. According to the literature, CSF outflow through the ONS exists.[20,22] Raykin et al.[23] measured the permeability of porcine ONS. They reported a permeability (κ) of 7.34e-5 mL/min/cm^2/mm Hg. If we know the area of the ONS we may calculate the outflow resistance across the ONS:

$$R_{ONS} = \frac{\Delta P}{Q} = \frac{1}{\kappa A} = \frac{1}{2\kappa\pi \bar{r}_{ONS} L_{ONSAS}}. \quad (5)$$

Radius and length were acquired from our MRI data and using an average radius of the ONSAS ($\bar{r}_{ONS}$) of 2.1 mm (supine value) and a length (L_{ONSAS}) of 2.6 cm (Table 1) the resulting equilibrium resistance was: $R_{ONS} = 3968$ mm Hg/(mL/min). Because this R_{ONS} value represents one eye, the total outflow resistance for two eyes in parallel becomes half of this value. In our model, CSF absorption across the ONS was driven by the pressure difference between the ONSAS and the intraorbital space (i.e., $P_{ONSAS} - P_{orb}$), and flow ceased if P_{ONSAS} dropped below P_{orb}.

Simulation Specifics and Main Outputs/Primary Variables. The main outputs of the mathematical model were the pressure in the ONSAS and cranial SAS at the level of the LC (P_{ONSAS} and ICP_{LC}, respectively), as well as the radius of the ONS (r_{ONS}). These variables were calculated during a posture change from *supine* to a *90° upright* position. The simulations started in supine and after 5 minutes we changed from supine to upright over a period of 10 seconds. The simulation was then continued for about 1 hour to ensure that we reached equilibrium (controlled by CSF formation and absorption). The simulated r_{ONS} in the upright position revealed where ONSAS collapse occurred, if at all, and the difference between ICP_{LC} and P_{ONSAS} revealed the resulting effects on the pressure communication along the ONSAS. All variables were calculated continuously over time. The simulations corresponded to a healthy subject with a supine equilibrium ICP of 11.2 mm Hg, which in turn corresponded to $ICP_{LC} = P_{ONSAS} = 7.4$ mm Hg. The model was implemented and solved numerically in Modelica (Open Source Modelica Consortium, OpenModelica 1.14.0, www.openmodelica.org).

We performed a sensitivity analysis for the distensibility by repeating the simulations with $D_i \pm 1 \cdot SD$. The *SD* was taken as the standard deviation of the measured distensibility values in Table 1, that is, $D_i \pm 0.005$ mm/mm Hg.

Statistics

Results are presented as mean ± SD unless otherwise specified. The Student's paired samples *t*-test was used to compare the ONSAS volume between body postures (significance level $\alpha = 0.05$). ICCs were used for the inter-rater agreement test regarding the segmentation of the ONSAS volumes (2-way random effects, absolute agreement, and single rater/measurement).

Results

MRI Measurements

For all 12 optic nerves, the ONSAS volume was 177 ± 45 µL and 118 ± 42 µL in HDT and HUT, respectively. This change reflected a significant decrease of 70 ± 28 µL in the ONSAS of the right optic nerve (from 192 ± 42 µL to 122 ± 47 µL, $P = 0.002$), and 48 ± 30 µL in the ONSAS of the left optic nerve (from 162 ± 46 µL to 114 ± 40 µL, $P = 0.012$). The corresponding hydrostatic pressure difference between the two postures was 10.6 ± 1.6 mm Hg. In Figure 3, the measured ONSAS volume per slice can be seen in both HDT and HUT, showing that the volume decreased along the

Investigative Ophthalmology & Visual Science

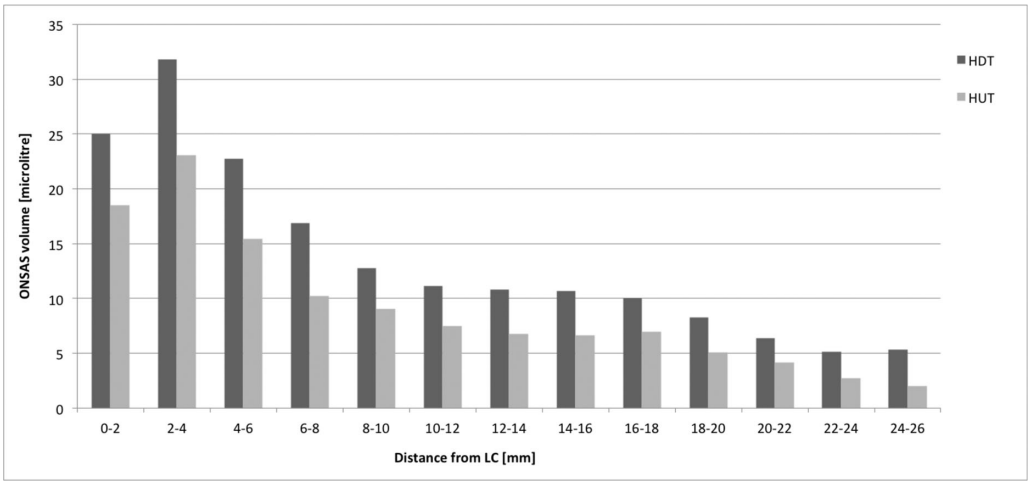

Figure 3. Average ONSAS volume per slice in the MRI data for all optic nerves. In all slices the volume decreased when changing from HDT to HUT.

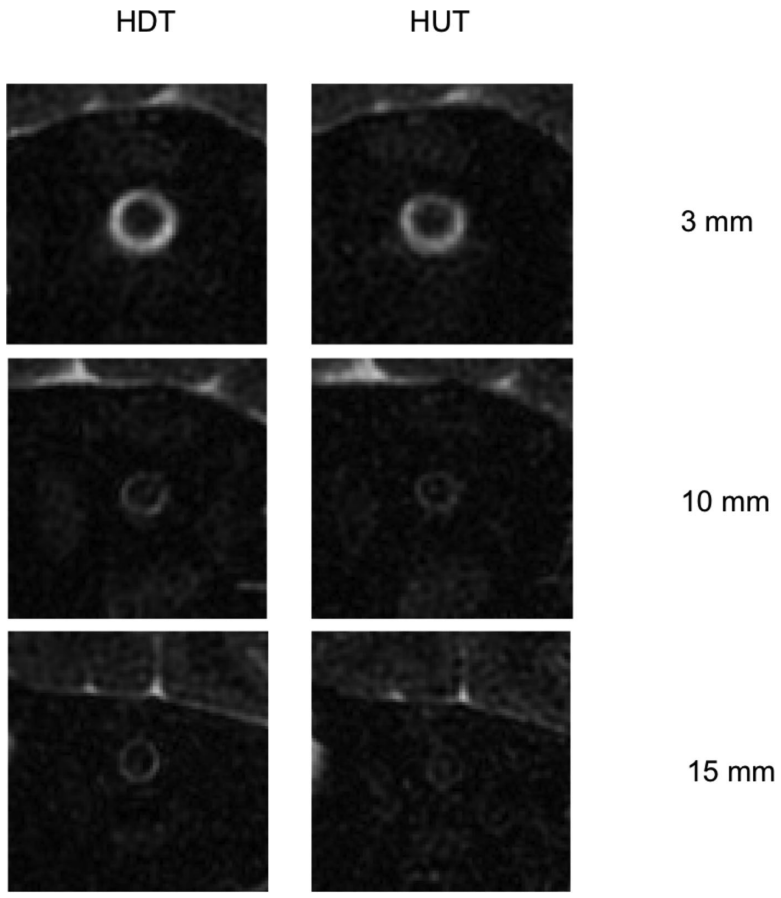

Figure 4. MRI of the ONSAS in a test subject in HDT and HUT 3, 10, and 15 mm behind LC. The ONSAS is annulus-shaped and visible in all images.

entire ONSAS. The largest volume and the largest change in volume were found in the bulbar region. Looking at the HUT MRIs, the ONSAS was still visible along the entire optic nerve in most subjects (for an example, see Fig. 4). However, in certain cases the ONSAS seemed to disappear in the orbital section in HUT, which may indicate an ONSAS

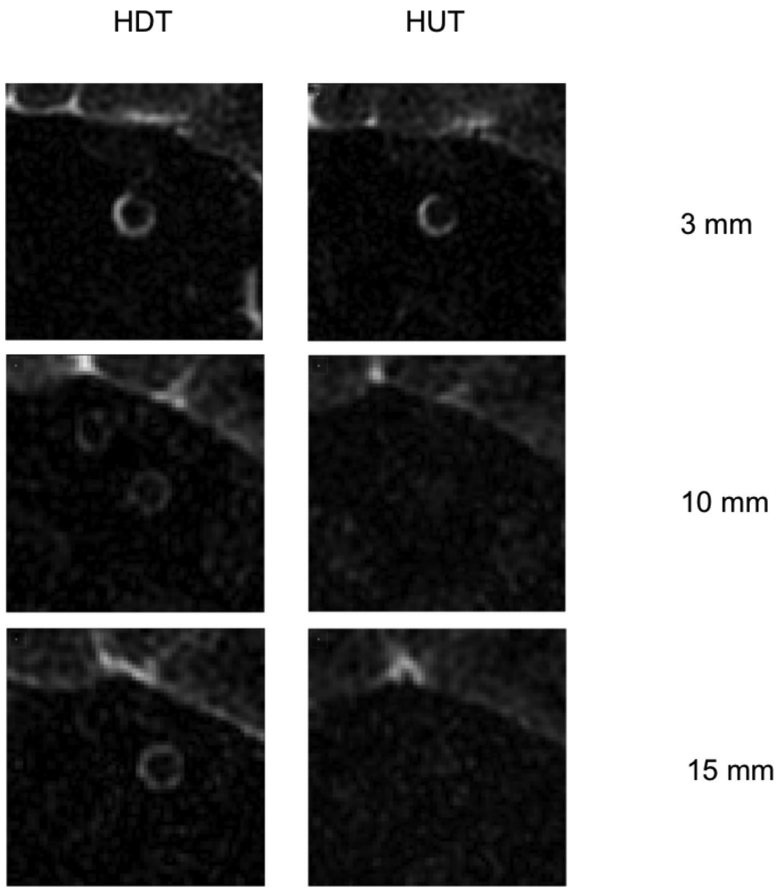

Figure 5. MRI of the ONSAS in a second subject in HDT and HUT 3, 10, and 15 mm behind LC. In HUT, the ONSAS is visible in the bulbar region only.

collapse already at 13° in these subjects (Fig. 5). The average distensibility along the optic nerve ($\bar{D}$) was estimated as 0.018 ± 0.011 mm/mm Hg (0.020 ± 0.010 mm/mm Hg for the right ONSAS and 0.015 ± 0.011 mm/mm Hg for the left ONSAS).

Simulations

Pressure. The P_{ONSAS} and ICP_{LC} are presented as a function of time in Figure 6A. In supine, the ICP_{LC} was 7.4 mm Hg and equaled P_{ONSAS}, indicating an open passage between the intracranial space and the ONSAS. After 5 minutes we simulated the change in body position (supine to upright) over a period of 10 seconds. This introduced a drop in both pressures. During the first 2 seconds, P_{ONSAS} decreased rapidly, before it slowed down because of collapse of the last segment ($i = 13$) of the ONSAS, disconnecting P_{ONSAS} from ICP_{LC}. Thereafter, P_{ONSAS} slowly reached its steady state value of –5.4 mm Hg, and the ICP_{LC} reached a steady state of –6.5 mm Hg.

The sensitivity analysis (Figs. 6B–C) showed that the increased ONS distensibility ($D_i + 1 \cdot SD$) yielded an early collapse with a steady state ONSAS pressure of $-$ 1.7 mm Hg, whereas for the decreased distensibility ($D_i - 1 \cdot SD$) there was no collapse and ICP_{LC} and P_{ONSAS} were nearly identical.

Figure 7 shows the ONSAS pressure as a function of ICP_{LC} for the three different distensibilities. For the decreased distensibility there is a linear relationship between the two for all pressures. For the baseline distensibility there is a linear relationship for pressures above –5.4 mm Hg, whereas below –5.4 mm Hg the ONSAS pressure was independent of ICP_{LC}, indicating that the ONSAS pressure reaches a constant value after ONSAS collapse, as the ONSAS is separated from the intracranial space. For the increased distensibility the ONSAS pressure becomes independent of ICP_{LC} already at –1.7 mm Hg.

Estimated TLCPD. Using the group average IOP, the TLCPD predicted by our model becomes: $TLCPD = IOP - P_{ONSAS} = (14.2 - 7.4)$ mm Hg = 6.8 mm Hg in supine, and 10.1 $-$ ($-$5.4) mm Hg = 15.5 mm Hg in upright. For a non-collapsible system (i.e., for the decreased distensibility), the TLCPD in the upright posture is only slightly higher 10.1 $-$ ($-$6.5) mm Hg = 16.6 mm Hg. The increased distensibility predicted a TLCPD of 11.8 mm Hg in upright postures, meaning that within the limits of our sensitivity analysis the collapse reduced the postural increase in the TLCPD by 0 to 4.8 mm Hg.

ONSAS Collapse. As we went from supine to upright, r_{ONS} decreased and the ONSAS collapsed 26 mm behind the LC in the upright position (Figs. 6D–E). In the remaining ONSAS segments the radius diminished, but the passage remained open (see Fig. 8 for a schematic image). Increasing the distensibility yielded a collapse at the same location (at 26 mm), whereas for the decreased distensibility the ONSAS remained open regardless of body posture (Fig. 6F).

Investigative Ophthalmology & Visual Science

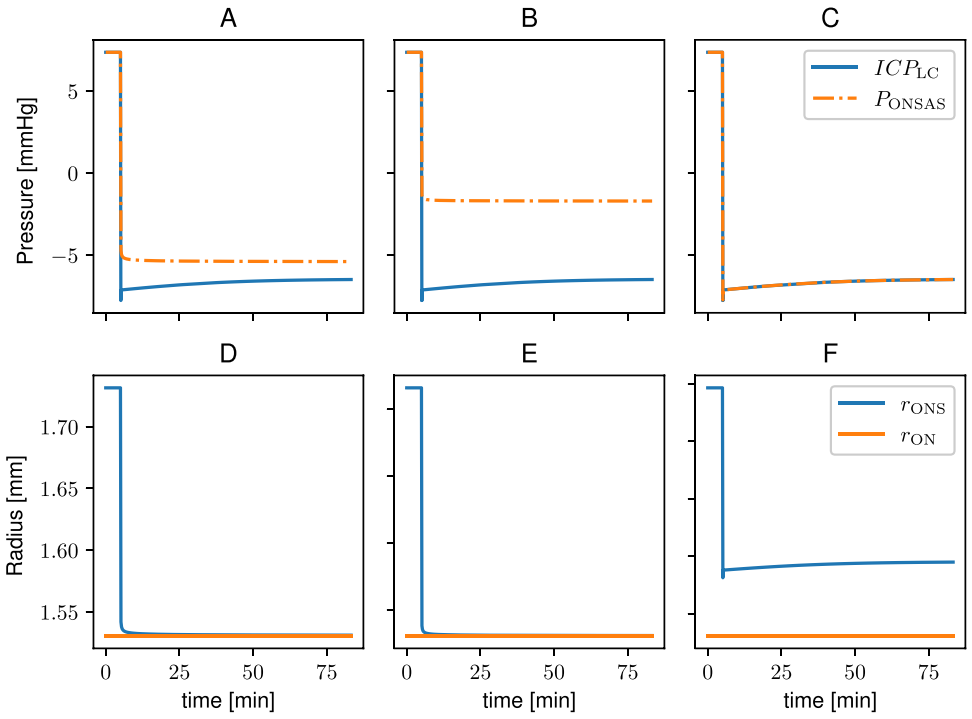

Figure 6. Plot of pressure (**A–C**) and minimum ONSAS radius (**D–F**) versus time when changing body position from supine to upright at time = 5 minutes. Each column corresponds to different degrees of ONS distensibility to illustrate the sensitive relationship between distensibility and predicted ONSAS collapse: (**A** & **D**) the distensibility directly acquired from the measurements (D_i), (**B** & **E**) represents increased distensibility ($D_i + 1 \cdot SD$), and (**C** & **F**) represents reduced distensibility ($D_i - 1 \cdot SD$). In the supine position, the ICP at the level of the eye (ICP_{LC}) equals the ONSAS pressure (P_{ONSAS}). In the upright posture, occlusion of the ONSAS causes a pressure difference in (**A**) and (**B**), whereas in (**C**) there is no occlusion, and the ICP equals the ONSAS pressure. Note that the pressure difference between the cranial and optic nerve SAS increases with increased distensibility.

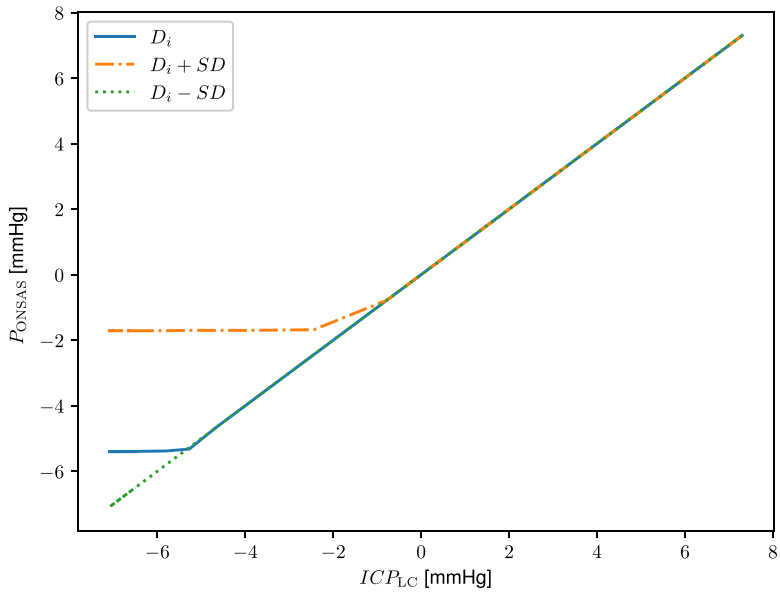

Figure 7. Plotting the ONSAS pressure as a function of the ICP for three different distensibility values. The curve shows a linear dependence when the ONSAS is open and that the ONSAS pressure is nearly constant after the collapse. For D_i the collapse happens at an ICP of –5.4 mm Hg, for $D_i + 1 \cdot SD$ the collapse happens at –1.7 mm Hg, and for $D_i - 1 \cdot SD$ there is no collapse and there is a linear relationship between ONSAS pressure and ICP all the way.

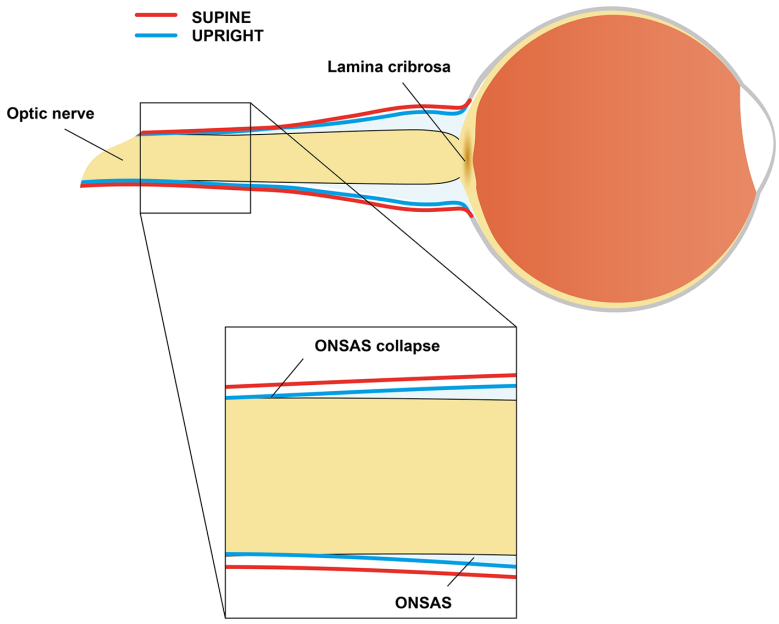

Figure 8. Computed radii for 0 deg supine (*red*) and 90 deg upright (*blue*) postures. The computed collapse occurred in the last segment (furthest away from the LC). The optic nerve shape is based on the MRI measurements.

ONSAS Axial Flow Rate. Because of the decrease in r_{ONS} and the accompanying increase in R_{ONSAS}, the simulated flow between the cranial SAS and the ONSAS was altered during the posture change. In supine equilibrium, a flow rate of roughly 2.2 µL/min was directed from the cranial SAS to the ONSAS and was absorbed through the ONS. In the upright posture, there was no flow through the ONS and the flow through the ONSAS was reversed, going *from* the ONSAS *toward* the cranial SAS. The magnitude of the flow rate slowly converged toward zero (it was <0.002 µL/min after 1 hour in upright). The flow rates were roughly the same for the increased distensibility (both in magnitude and direction), whereas for the decreased distensibility the flow was roughly 0.01 µL/min after 1 hour in upright and the direction of flow remained the same as in the supine position.

Discussion

The present study revealed a posture-dependent change in ONSAS volume along the optic nerve measured by MRI in healthy subjects. The simulations predicted an ONSAS collapse in the upright posture and a disrupted communication between the ONSAS and cranial SAS. The effects on the TLCPD were sensitive to the ONS distensibility.

ONSAS Collapse

Previous studies have managed to detect a change in the ONSAS diameter between horizontal and upright postures in patients with intracranial hypotension and CSF leakages but not in healthy controls.[24–26] However, these studies all used ultrasound and were limited to measurements in the bulbar ONSAS 3 mm behind the LC. Our MRI results include the entire ONSAS and indicate that a collapse of the orbital ONSAS may be plausible even in healthy subjects. The ONSAS collapse was supported both by the MRIs, in which the ONSAS visually disappeared in certain subjects already at an HUT of 13° (Fig. 5), and by our mathematical model, which predicted a collapse in the upright posture (Fig. 6). Both the collapse directly observed in the MRIs and the collapse predicted by the model occurred in the orbital section of the optic nerve (Figs. 5 and 8), despite the largest diameter changes occurring in the bulbar section (Fig. 3).

A disrupted communication between the cranial SAS and the ONSAS (assessed in horizontal positions) has been linked to ocular diseases, including normal tension glaucoma[27–29] and papilledema,[30] indicating ONSAS collapse in supine as a sign of disturbed ONSAS dynamics. Because our model predicts a general collapse in the upright posture, our results suggest that the normal physiology of the ONSAS is similar to that of the jugular veins, with an open communication in horizontal postures and a collapse in vertical postures.[31–33] This opens the possibility that the absence rather than the occurrence of a collapse could prove detrimental to ocular physiology in upright postures. These findings motivate further studies of the ONSAS in supine and upright postures both in normal physiology and pathophysiology.

TLCPD

Simultaneous measurements of IOP and ICP in supine, sitting, and HDT have shown that the ICP is more sensitive to body posture than IOP, leading to a posture-dependent TLCPD.[7,34] These studies assumed a fully communicating ONSAS and did not take a potential ONSAS collapse into account. In the current study, the collapsible ONSAS disrupted the link between ICP and ONSAS pressure, preventing the ONSAS pressure from dropping to the same level as the ICP in the upright posture (Fig. 6), suggesting that the postural change in the TLCPD is not as large as previous studies suggested. The results support the collapse as a possible safety mechanic against large TLCPDs in the upright posture,[5] with the effectiveness of the safety

Investigative Ophthalmology & Visual Science

mechanism being highly sensitive to the ONS distensibility (Fig. 7). This could have direct bearing on various TLCPD-related diseases as differences in the distensibility between individuals or groups of individuals could lead to substantially different TLCPDs. One example is glaucoma, specifically normal tension glaucoma, in which a high TLCPD is believed to be an underlying cause.[1–4] A decreased distensibility would result in a lower ICP and an increased TLCPD in the upright posture and could thus contribute to the development of the disease. Such a decrease in distensibility could occur naturally with aging, as the dura mater stiffens as we grow older,[35] eventually compromising the postural ONSAS collapse and increase the risk of developing glaucoma. Another ocular disease related to the TLCPD is the spaceflight-associated neuro-ocular syndrome that develops in astronauts on extended spaceflights, in which the clinical findings include globe flattening, choroidal folds, and papilledema, not unlike findings in patients with increased ICP.[8] To explain these clinical findings it has been suggested that microgravity eliminates the ICP reduction provided by the upright posture on earth, leading to a chronic increase in ICP in microgravity[7,9] and thus a decrease in the TLCPD and an increased force posterior to the eye. If there is an ONSAS collapse in the upright posture, the effect of this chronic increase in ICP on the TLCPD will be less and less with increasing ONS distensibility.

The extended modeling of the CSF system including the ONS pathway and the posture dependency also has potential implications for studying the glymphatic system of the brain,[36] which if impaired is thought to be a part of the development of Alzheimer's disease.[37] This system is considered to be involved in removal of brain metabolites and was also recently described to transport metabolites from the intraocular space through the optic nerve head to the ONSAS, and it was suggested that this glymphatic pathway of the eye might be impaired in glaucoma.[38] Understanding the role of ONSAS/SAS communication, incorporating body position and collapse function, may thus contribute with valuable insights essential for the exploration of glymphatic pathways and their driving pressure gradients.

We did not directly measure the ONSAS pressure in this study. However, our results can be compared with experimental results in animals, showing an ONSAS closing pressure ranging from a few millimeters of mercury above to a few millimeters of mercury below zero when altering the CSF pressure artificially.[11,12] Furthermore, Morgan et al.[12] showed a relationship between CSF and ONSAS pressure in dogs that was very similar to our Figure 7, with the ONSAS pressure plateauing close to –1 mm Hg (although with some variability), compared with our plateau at –1.7 mm Hg for the increased distensibility. In other words, increasing the distensibility with 1 SD yielded results comparable to experiments. Thus it is likely that a collapse of the ONSAS will affect the ONSAS pressure, at least to some degree, and therefore also reduce the effects of posture on the TLCPD.

Limitations

As we did not have access to an upright/sitting MRI scanner, we could not measure the ONSAS in 90° by MRI. In addition, the MRI sequence was optimized to focus on the orbital section of the optic nerve, leading to uncertainties for cases in which the optic nerve was highly tortuous, although this problem applies to both postures equally.

The simulated ONSAS flows from our model are dependent on the outflow across the ONS, a quantity never measured directly. Furthermore, we neglected the finer structures in the ONSAS.[39] These structures connect the pia around the optic nerve to the arachnoid membrane and could have an impact on the proposed collapse.

Conclusions

The ONSAS volume along the optic nerve was shown to be posture dependent. The simulations supported an ONSAS collapse in the upright posture, motivating further research to validate its applicability both in normo- and pathophysiology. The TLCPD was sensitive to variations in ONS distensibility, meaning that even small changes in optic nerve stiffness, for example, potential changes occurring with aging, could yield highly different TLCPDs in the upright posture.

Acknowledgments

The authors thank x-ray technician/nurse Rebeca Peredo de Axelsson for skillful assistance with planning and execution of the MRI investigations.

Supported by the Swedish National Space Board (Grant no. 193/17), Swedish Foundation for Strategic Research, the Knut and Alice Wallenberg Foundation, and the Swedish Society for Medical Research.

Disclosure: **P. Holmlund**, None; **K.-H. Støverud**, None; **A. Wåhlin**, None; **U. Wiklund**, None; **J. Malm**, None; **G. Jóhannesson**, None; **A. Eklund**, None

References

1. Berdahl JP, Fautsch MP, Stinnett SS, Allingham RR. Intracranial pressure in primary open angle glaucoma, normal tension glaucoma, and ocular hypertension: a case-control study. *Invest Ophthalmol Vis Sci*. 2008;49:5412–5418.
2. Ren R, Jonas JB, Tian G, et al. Cerebrospinal fluid pressure in glaucoma: a prospective study. *Ophthalmology*. 2010;117:259–266.
3. Lindén C, Qvarlander S, Jóhannesson G, et al. Normal-tension glaucoma has normal intracranial pressure: a prospective study of intracranial pressure and intraocular pressure in different body positions. *Ophthalmology*. 2018;125:361–368.
4. Guy AH, Wiggs JL, Turalba A, Pasquale LR. Translating the low translaminar cribrosa pressure gradient hypothesis into the clinical care of glaucoma. *Semin Ophthalmol*. 2016;31:131–139.
5. Johannesson G, Eklund A, Linden C. Intracranial and intraocular pressure at the lamina cribrosa: gradient effects. *Curr Neurol Neurosci Rep*. 2018;18:25.
6. Fleischman D, Allingham RR. The role of cerebrospinal fluid pressure in glaucoma and other ophthalmic diseases: a review. *Saudi J Ophthalmol*. 2013;27:97–106.
7. Eklund A, Johannesson G, Johansson E, et al. The pressure difference between eye and brain changes with posture. *Ann Neurol*. 2016;80:269–276.
8. Mader TH, Gibson CR, Pass AF, et al. Optic disc edema, globe flattening, choroidal folds, and hyperopic shifts observed in astronauts after long-duration space flight. *Ophthalmology*. 2011;118:2058–2069.
9. Lawley JS, Petersen LG, Howden EJ, et al. Effect of gravity and microgravity on intracranial pressure. *J Physiol*. 2017;595:2115–2127.

10. Wåhlin A, Holmlund P, Fellows AM, Malm J, Buckey JC, Eklund A. Optic nerve length before and after spaceflight. *Ophthalmology*. 2021;128:309–316.
11. Hou R, Zhang Z, Yang D, et al. Intracranial pressure (ICP) and optic nerve subarachnoid space pressure (ONSP) correlation in the optic nerve chamber: the Beijing Intracranial and Intraocular Pressure (iCOP) study. *Brain Res*. 2016;1635:201–208.
12. Morgan WH, Yu DY, Alder VA, et al. The correlation between cerebrospinal fluid pressure and retrolaminar tissue pressure. *Investig Ophthalmol Vis Sci*. 1998;39:1419–1428.
13. Moller PM. The pressure in the orbit. *Acta Ophthalmol Suppl*. 1955;(suppl 43):1–100.
14. Xie X, Zhang X, Fu J, et al. Noninvasive intracranial pressure estimation by orbital subarachnoid space measurement: the Beijing Intracranial and Intraocular Pressure (iCOP) study. *Crit Care*. 2013;17:R162.
15. Weigel M, Lagreze WA, Lazzaro A, Hennig J, Bley TA. Fast and quantitative high-resolution magnetic resonance imaging of the optic nerve at 3.0 tesla. *Invest Radiol*. 2006;41:83–86.
16. Gehlen M, Kurtcuoglu V, Schmid Daners M. Is posture-related craniospinal compliance shift caused by jugular vein collapse? A theoretical analysis. *Fluids Barriers CNS*. 2017;14:5.
17. Davson H. Formation and drainage of the cerebrospinal fluid. *Sci Basis Med Annu Rev*. 1966:238–259.
18. Qvarlander S, Sundström N, Malm J, Eklund A. Postural effects on intracranial pressure: modeling and clinical evaluation. *J Appl Physiol*. 2013;115:1474–1480.
19. Holmlund P, Eklund A, Koskinen L-OD, et al. Venous collapse regulates intracranial pressure in upright body positions. *Am J Physiol Regul Integr Comp Physiol*. 2018;314:R377–R385.
20. Killer HE, Laeng HR, Groscurth P. Lymphatic capillaries in the meninges of the human optic nerve. *J Neuroophthalmol*. 1999;19:222–228.
21. Kaskar OG, Fleischman D, Lee YZ, Thorp BD, Kuznetsov AV, Grace L. Identifying the critical factors governing translaminar pressure differential through a compartmental model. *Investig Opthalmology Vis Sci*. 2019;60:3204.
22. Lüdemann W, von Rautenfeld DB, Samii M, Brinker T. Ultrastructure of the cerebrospinal fluid outflow along the optic nerve into the lymphatic system. *Childs Nerv Syst*. 2005;21:96–103.
23. Raykin J, Best L, Gleason R, et al. Optic nerve sheath mechanics and permeability in VIIP syndrome. *Invest Ophthalmol Vis Sci*. 2014;55:4591.
24. Ertl M, Aigner R, Krost M, et al. Measuring changes in the optic nerve sheath diameter in patients with idiopathic normal-pressure hydrocephalus: a useful diagnostic supplement to spinal tap tests. *Eur J Neurol*. 2017;24:461–467.
25. Fichtner J, Ulrich CT, Fung C, et al. Management of spontaneous intracranial hypotension–transorbital ultrasound as discriminator. *J Neurol Neurosurg Psychiatry*. 2016;87:650–655.
26. Fichtner J, Ulrich CT, Fung C, et al. Sonography of the optic nerve sheath diameter before and after microsurgical closure of a dural CSF fistula in patients with spontaneous intracranial hypotension–a consecutive cohort study. *Cephalalgia*. 2019;39:306–315.
27. Boye D, Montali M, Miller NR, et al. Flow dynamics of cerebrospinal fluid between the intracranial cavity and the subarachnoid space of the optic nerve measured with a diffusion magnetic resonance imaging sequence in patients with normal tension glaucoma. *Clin Exp Ophthalmol*. 2018;46:511–518.
28. Pircher A, Montali M, Berberat J, Remonda L, Killer HE. The optic canal: a bottleneck for cerebrospinal fluid dynamics in normal-tension glaucoma? *Front Neurol*. 2017;8:47.
29. Killer HE, Miller NR, Flammer J, et al. Cerebrospinal fluid exchange in the optic nerve in normal-tension glaucoma. *Br J Ophthalmol*. 2012;96:544–548.
30. Killer HE, Jaggi GP, Miller NR, et al. Cerebrospinal fluid dynamics between the basal cisterns and the subarachnoid space of the optic nerve in patients with papilloedema. *Br J Ophthalmol*. 2011;95:822–827.
31. Valdueza JM, von Munster T, Hoffman O, Schreiber S, Einhaupl KM. Postural dependency of the cerebral venous outflow. *Lancet*. 2000;355:200–201.
32. Dawson EA, Secher NH, Dalsgaard MK, et al. Standing up to the challenge of standing: a siphon does not support cerebral blood flow in humans. *Am J Physiol - Regul Integr Comp Physiol*. 2004;287:911–914.
33. Holmlund P, Johansson E, Qvarlander S, et al. Human jugular vein collapse in the upright posture: implications for postural intracranial pressure regulation. *Fluids Barriers CNS*. 2017;14:17.
34. Jasien JV, Samuels BC, Johnston JM, Downs JC. Effect of body position on intraocular pressure (IOP), intracranial pressure (ICP), and translaminar pressure (TLP) via continuous wireless telemetry in nonhuman primates (NHPs). *Invest Ophthalmol Vis Sci*. 2020;61:18.
35. Zwirner J, Scholze M, Waddell JN, Ondruschka B, Hammer N. Mechanical properties of human dura mater in tension–an analysis at an age range of 2 to 94 years. *Sci Rep*. 2019;9:16655.
36. Iliff JJ, Wang M, Liao Y, et al. A paravascular pathway facilitates CSF flow through the brain parenchyma and the clearance of interstitial solutes, including amyloid beta. *Sci Transl Med*. 2012;4:147ra111.
37. Xu Z, Xiao N, Chen Y, et al. Deletion of aquaporin-4 in APP/PS1 mice exacerbates brain Aβ accumulation and memory deficits. *Mol Neurodegener*. 2015;10:58.
38. Wang X, Lou N, Eberhardt A, et al. An ocular glymphatic clearance system removes β-amyloid from the rodent eye. *Sci Transl Med*. 2020;12:eaaw3210.
39. Killer HE, Laeng HR, Flammer J, Groscurth P. Architecture of arachnoid trabeculae, pillars, and septa in the subarachnoid space of the human optic nerve: anatomy and clinical considerations. *Br J Ophthalmol*. 2003;87:777–781.

Amended April 22, 2021: When the article was first published, in the "Estimated TLCPD" section of the Results, two numbers were shown as positive that should have been negative. The equation 10.1 − 5.4 mm Hg = 15.5 mm Hg has now been corrected to 10.1 − (−5.4) mm Hg = 15.5 mm Hg, and the equation 10.1 − 6.5 mm Hg = 16.6 mm Hg has been corrected to 10.1 − (−6.5) mm Hg = 16.6 mm Hg.

Investigative Ophthalmology & Visual Science